Degradation of $(La_{0.6}Sr_{0.4})_{0.95}(Co_{0.2}Fe_{0.8})O_{3-\delta}$ Solid Oxide Fuel Cell Cathodes at the Nanometre Scale and Below

Na Ni[1*], Samuel J. Cooper[1], Robert Williams[2], Nils Kemen[1], David W. McComb[2] and Stephen J. Skinner[1]

[1] Imperial College London, Exhibition road, SW7 2AZ London UK
[2] Center for Electron Microscopy and Analysis, Ohio State University, 1305 Kinnear Road, Columbus, OH 43212, USA
*n.ni@imperial.ac.uk

Abstract: The degradation of intermediate temperature solid oxide fuel cell (ITSOFC) cathodes has been identified as a major issue limiting the development of ITSOFCs as high efficiency energy conversion devices. In this work, the effect of Cr poisoning on $(La_{0.6}Sr_{0.4})_{0.95}(Co_{0.2}Fe_{0.8})O_{3-\delta}$ (LSCF6428), a particularly promising ITSOFC cathode material, was investigated on symmetrical cells using electrochemical impedance spectroscopy and multi-scale structural/chemical analysis by advanced electron and ion microscopy. The systematic combination of bulk and high-resolution analysis on the same cells allows, for the first time, to directly correlate Cr induced performance degradation with subtle and localized structural/chemical changes of the cathode down to the atomic scale. Up to two orders of magnitude reduction in conductivity, oxygen surface exchange rate and diffusivity were observed in Cr poisoned LSCF6428 samples. These effects are associated with the formation of nanometer size $SrCrO_4$; grain boundary segregation of Cr; enhanced B-site element exsolution (both Fe and Co); and reduction in the Fe valence, the latter two being related to Cr substitution in LSCF. The finding that significant degradation of the cathode happens before obvious microscale change points to new critical SOFC degradation mechanisms effective at the nanometer scale and below.

1. Introduction

As a device that directly converts the chemical energy of gaseous fuels to electricity through electrochemical processes, solid oxide fuel cells (SOFCs) have become of great interest as a potential means of clean and efficient electricity production. The large-scale commercialization of SOFCs is currently constrained by a

combination of cost and durability issues. In order to address these concerns, much effort have been focused on reducing the cell operating temperature from conventionally ~ 1000 °C to below 800 °C [1]. For the intermediate-temperature SOFCs (ITSOFCs), metallic materials have become a preferential choice for the cell interconnect due to their excellent physical and chemical properties. However, almost all commonly used metallic alloys have a significant chromium content, which has been found to cause poisoning of the cathode under operating conditions. Sources of Cr species can also come from stainless steel components found in the balance-of-plant (BoP) such as heat exchangers[2]. This poisoning has been found to lead to rapid electrochemical performance degradation of the cathodes [3-6], including $(La,Sr)(Co,Fe)O_{3-\delta}$ (LSCF) perovskite oxides, which are considered to be a promising cathode material for ITSOFCs due to their significantly higher electrochemical activity for the O_2 reduction reaction and higher oxygen ion conductivity than the conventional $(La,Sr)MnO_3$ (LSM) cathode[7].

Cr poisoning is generally deemed to be caused by the reduction of volatile Cr (VI) species to solid Cr species, which can deposit at the cathode surface or the cathode/electrolyte/gas triple phase boundaries (TPBs) via vapor phase and/or solid state transportation[8]. Studies on the mechanisms of Cr deposition have proposed that the process is a chemical reaction between Cr (VI) with active elements in the electrode material such as Sr in LSCF[8-9], more than an electrochemical reduction process in competition with O_2 reduction[10-11]. The Cr rich phases, in the case of LSCF, have been suggested to be mainly $SrCrO_4$ with a minor Cr_2O_3 impurity from bulk analysis using X-ray diffraction (XRD) and scanning electron microscopy/energy-dispersive X-ray spectroscopy (SEM/EDX)[8, 12-13]. Many studies have reported that Cr deposition tends to occur at the LSCF surface[6, 8-9, 12], in contrast to LSM where the Cr deposition is

concentrated at the LSM/electrolyte interface[9, 14]. As a result, it has been proposed that the poisoning effect is mainly due to the formation of the large $SrCrO_4$ deposits (up to ~6 μm) that have poor electrical conductivity and block the surface pores of the electrode layer[8]. However, uniform distribution of Cr throughout the entire LSCF cathode at the micrometer scale has also been reported[14-16]. Also, it was reported that homogeneous Cr distribution with lower deposited Cr content at the LSCF cathode surface showed greater degradation than cathodes with a larger quantity of Cr surface deposits, but lower Cr content inside the cathode[17]. Therefore, it is likely that there exist other degradation mechanisms involving the interaction of Cr with LSCF beyond the surface region and at a finer scale, as suggested for some other electrode materials (LSM [18], $La_{0.8}Sr_{0.2}CoO_3$ (LSC) [19], $(La,Sr)MnO_3$-$(Zr,Y)O_2$ [20] and $LaNi_{0.6}Fe_{0.4}O_3$ [21]). For LSCF, some attempts employing transmission electron microscopy (TEM) have been made to study Cr poisoning at the nanometer scale[16, 22-24]. However, due to the difficulty associated with TEM sample preparation from highly porous electrodes and the complexity of the materials chemistry, the few TEM analysis avalaible in the literature has been very preliminery with only limited level of details and accuracy, and even missintepreation of the data in some cases. More careful studies able to provide much more accurate and detailed high-resolution information are needed for a better understanding of the fundamental poisoning mode of Cr in LSCF cathodes, as the Cr behaviour is likely to be vey inhomogenous and localized.

Electrochemical impedance spectroscopy (EIS) has been used widely to characterize the electrochemical properties of SOFC electrodes and microstructure is often a focus of electrode characterization; however, a combination of the two, especially with detailed (sub-)nanoscale structural/chemical investigation for Cr poisoning of LSCF cathodes, is missing in the literature, partly due to the above

mentioned difficulties associated with high-resolution analysis of the porous and complicated system. In this work, we aim for a more fundamental understanding of the intrinsic Cr interaction with LSCF related to its poisoning. Cr poisoning of the $(La_{0.6}Sr_{0.4})_{0.95}(Co_{0.2}Fe_{0.8})O_{3-\delta}$ cathode (LSCF6428) was studied systematically by carrying out combined bulk impedance analysis and detailed multi-scale structural and chemical investigation with advanced ion and electron microscopy on the same LSCF6428/$Ce_{0.9}Gd_{0.1}O_{2-x}$ (CGO)/LSCF6428 symmetrical cell samples. With our ability of preparing high-quality TEM specimens from the porous structure and effectively combining multiple TEM techniques to extract complementary and quantitative information, we were able to reveal the structural and chemical origins, at the nanoscale and below, of the LSCF performance degradation, and showed for the first time new Cr incorporation behavior including grain boundary Cr segregation and Co deficiency, and Cr substitution in the LSCF lattice leading to the localized change of LSCF stoichiometry and B-site valence. These findings revealed new critical degradation mechanisms that will provide valuable insight for the development of poisoning resistant cathode materials.

2. Experimental Section

2.1 Electrochemical cell preparation

Symmetric cells with LSCF6428 on a $Ce_{0.9}Gd_{0.1}O_{2-x}$ (CGO) electrolyte were prepared by screen printing LSCF6428 ink (Fuel Cell Materials, Lewis Center, OH, USA) on both sides of the CGO pellets prepared by pressing and sintering (details in the Supporting Information). The cells were then sintered at 1100 °C for 2 h in air with heating rate and a cooling rate of 5 °C min^{-1}. The LSCF6428 thickness was ~ 20 μm as determined by SEM from the cross sections of the samples (Figure S1).

4

2.2 Cr poisoning

The chemical reaction between Cr species and the cathode material has been proposed to be a main poisoning mechanism in the literature[4, 8-9] and the objective of the work is to develop both the methodology and a fundamental understanding of the poisoning mechanisms by investigating the correlation between the material degradation and the intrinsic Cr/LSCF interaction modes operating at the nanometer scale and below. As a result, the poisoning strategy adopted in this work was impregnating the LSCF 6428 cathode with a Cr stock solution of 1.22 mol l^{-1} as employed in a previous study[5], in order to allow for a direct reaction between Cr species and LSCF that could lead to a rapid and significant poisoning effect. The details are described in the Supporting Information. The impregnated sample was then heated at 900 °C for 5 hours to allow for reactions between Cr and LSCF. The slightly higher temperature than typical ITSOFC operating temperatures was also chosen to accelerate the reactions and poisoning. SEM-EDX on the electrode reveals an overall Cr content of ~ 2.7 at.% as a result of the poisoning process. Reference samples without Cr impregnation were prepared and heat treated in the same condition and investigated as a reference. SEM-EDX confirmed the absence of Cr in the reference sample.

2.3 Characterization

2.3.1 EIS

EIS on the symmetric cell was measured at nominal temperatures from 600 to 900°C at 50° intervals in an electrochemical analysis apparatus (Probostat, Norecs, Norway) using a frequency response analyzer (Solartron Modulab). The actual temperature was recorded by a thermocouple placed close to the specimen. Impedance

measurements were made over the frequency range of 0.01 Hz to 1Mhz with 30 points per decade and an AC perturbation of 100 mV.

2.3.2 Characterization of bulk samples

Characterization of the bulk sample was carried out using scanning electron microscopy (SEM, LEO Gemini 1525 equipped with an energy-dispersive X-ray spectroscopy (EDX) detector) and X-ray diffraction (XRD, Bruker D2 PHASER desktop diffractometer using Cu-Kα radiation in the 2θ range 20°- 90°, with a step size of 0.0334° and a count time at each step of 1 s).

In order to obtain more detailed microstructural information, Focused Ion Beam Scanning Electron Microscopy (FIB-SEM) tomography of the LSCF6428 electrode was carried out using a dual beam system (Zeiss Auriga FIB-SEM). This allowed several of the microstructural parameters required for impedance analysis, such as the porosity, ε; surface area, A; and tortuosity factors, τ, to be extracted. The samples were first infiltrated with a commercial embedding resin (Epon_812 substitute, MNA, DDSA and DMP, Sigma-Aldrich Co. LLC, Dorset, UK) in order to obtainimproved contrast in individual SEM images (see Supporting Information). The FIB was operated using Ga^+ ions with an accelerating voltage of 30 kV for milling and 5 kV for imaging. The resulting voxel (3D pixel) size was c. 35 nm × 35 nm ×27 nm, and the total volume of the 3D stack was c. 1800 μm^3. Alignment, segmentation and statistical analysis of the 3D image data was performed using the Avizo software package (Visual Sciences Group, Bordeaux, France). The tortuosity factors of the electrode were estimated from the reconstructed 3D volume using a finite-difference steady-state diffusion simulation developed in-house (see Supporting Information for the details of the method).

2.3.3 TEM analysis

TEM analysis down to the atomic scale structure and chemistry was carried out on a JEOL 2100F microscope operating at 200 kV equipped with a 80 mm silicon drift EDX detector and a Gatan Tridiem imaging filter for EELS, a FEI Titan™ 80-300 microscope operated at 300 kV equipped with a field emission electron gun, a monochromator, a Cs-image corrector and Gatan Tridiem 866 imaging filter, and a FEI Titan³™ 60–300 microscope operated at 300 kV equipped with a high-coherence, high-brightness field emission electron gun (X-FEG), a Cs-image corrector, a monochromator, a Gatan Enfina spectrometer as well as a high-speed, high-throughput, quad-silicon drift detector (Super-X), optimized for rapid X-ray collection. Post-processing X-ray analysis was performed using Aztec (Oxford Instruments, UK) and Esprit (Bruker Nano GmbH, Berlin, Germany). The STEM probe size used for EDX mapping was between 0.15-0.5 nm and the EELS energy resolution was varied between 0.8 and 2 eV depending on the experimental conditions used, defined as the full width at half-maximum of the zero-loss peak (ZLP). TEM foils were prepared from the LSCF6428 porous layer by FIB milling using a Helios NanoLab 600 instrument (2–30 keV Ga^+ incident beam energy with currents of 16 pA - 21nA). The specimens were FIB polished at the last stage with 5 keV and then 2 keV Ga^+ to reduce the damage caused by the high energy Ga^+ beam.

Experimental Cliff & Lorimer k factors were obtained from standards to improve the EDX and EELS quantification in TEM. To analyze the B-site valence, the common white-line ratio method [25-26] that relates the transition metal white line ratios (L_3/L_2) in EELS with their valences was employed. Details on the measurement of k factors and white-line ratio are described in the Supporting Information.

3. Results and Discussion

3.1 Electrochemical degradation of the cathode

The impedance spectra of the reference sample (Cr free) and the Cr poisoned sample obtained at 780 °C and 600 °C are shown in Figure 1. The impedance data were fitted using an equivalent circuit composed of an inductance, L, resulting from the instrumentation, an ohmic resistance, R_o, and two RQ elements (a resistor in parallel with a constant phase element), as shown in the inset in Figure 1a. The fitting results for all measurements are shown in Table S1.
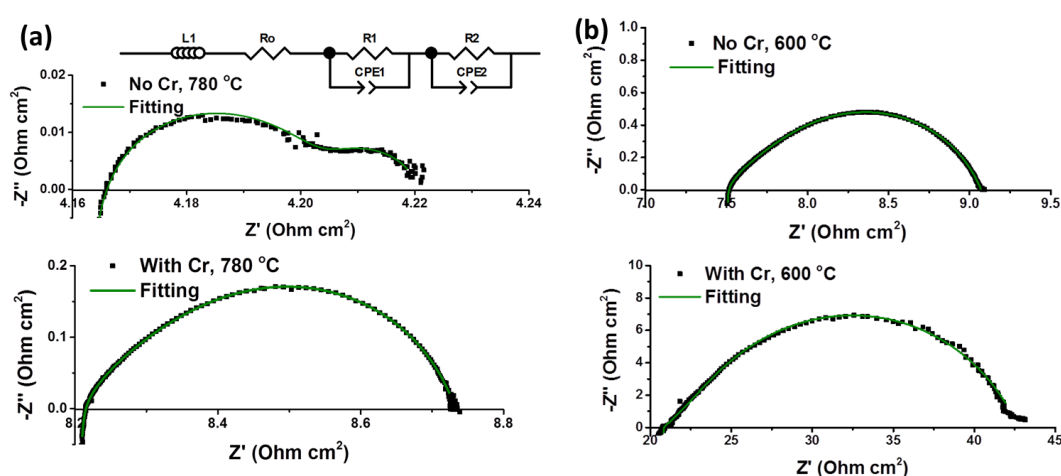

Figure 1 Representative impedance spectra of LSCF6428 cathodes with/without Cr poisoning at (a) 780 °C and (b) 600 °C. The impedance is normalized to the total electrode area (ohm cm²).

For the Cr free reference sample, the capacitances associated with the low frequency arc obtained from fitting at higher temperatures (690-780°C) are between 2.74 and 6.45 F cm^{-2}. Such a large capacitance is unlikely to be from any electrochemical process and is attributed to the gas phase diffusion process[27]. Apart from this low frequency arc seen at higher temperatures for the Cr free sample, all other measured impedance for both samples exhibit associated capacitances in the range of 10^{-2} to 10^{-3} F cm^{-2}. These impedances are therefore assumed to result mainly from the oxygen exchange at the electrode surface and oxygen lattice diffusion through the electrode [28-29]. The total electrode resistance related with the oxygen reduction process

8

$R_{electrode}$, was then regarded to be R_1+R_2 for most of the cases, but only R_1 for the Cr free samples measured at higher temperatures, where R_2 is the gas phase diffusion impedance (Table S1 and Figure 2a). It can be seen that the Cr poisoning has significantly degraded the LSCF6428 electrode, indicated by the increase in $R_{electrode}$ by more than one order of magnitude for the Cr poisoned sample compared to the reference. In addition, the disappearance of the gas diffusion resistance has also been suggested to be correlated with poor electrode performance[27]. The activation energy for the electrode process before and after Cr poisoning is similar, being 1.55±0.02 and 1.61±0.01 eV respectively, which is in good agreement with a previous study on similar LSCF electrodes (1.54 eV) [7] and Cr poisoned LSCF using the same approach as here (1.50 eV) [5].
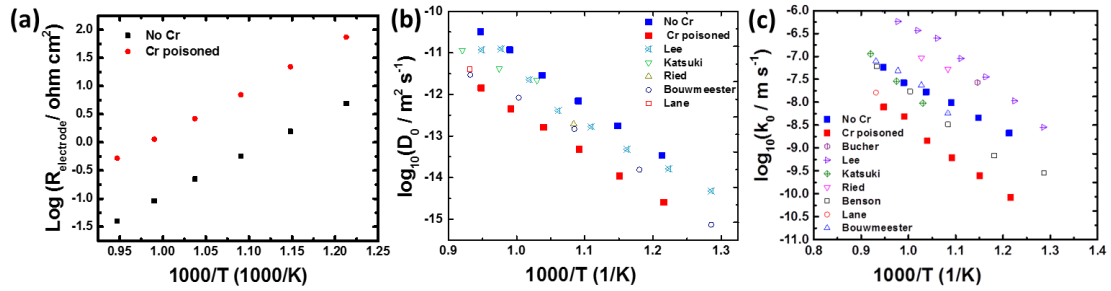

Figure 2 Arrhenius plots of the temperature dependence of (a) the cathode resistance $R_{electrode}$, (b) oxygen diffusion coefficient D_0 and (c) the oxygen surface reaction equilibrium exchange rate constant k_0. Literature data on D_0 and k_0 are shown for comparison.

The impedance spectra corresponding with $R_{electrode}$ has the asymmetrical characteristic shape of the Gerischer impedance, which is expected for a mixed conducting cathode such as LSCF. This can be analyzed by the Adler-Lane-Steele (ALS) model[30] for mixed conducting cathodes assuming the impedance is dictated by oxygen exchange at the electrode surface and solid state diffusion of oxygen in the electrode, as suggested by the capacitance values associated with $R_{electrode}$. In this case, the impedance can be expressed as:

9

$$Z_{electrode} = R_{electrode}\sqrt{\frac{1}{1-j\omega t_{electrode}}} \qquad (1)$$

where $t_{electrode}$ is the characteristic relaxation time related to the process. $R_{electrode}$ and $t_{electrode}$ can be written in the following form using oxygen transport and microstructural parameters:

$$R_{electrode} = \frac{RT}{2F^2}\sqrt{\frac{\tau}{(1-\varepsilon)ac_O^2 D_0 k_0}} \qquad (2)$$

$$t_{electrode} = \frac{(1-\varepsilon)c_V}{ac_O f_{thermo} k_0} \qquad (3)$$

where D_0 and k_0 are the oxygen diffusion coefficient and the oxygen surface reaction equilibrium exchange rate constant for LSCF, C_O the molar concentration of oxygen ions in LSCF, ε the porosity (pore volume fraction), τ the tortuosity of the solid phase, a the solid surface area per unit volume and f_{thermo} the so-called thermodynamic factor for the vacancies. For the Gerischer impedance, $t_{electrode}$ is related with the frequency at which the imaginary impedance is maximum (f_{max}) by $t_{electrode} \times f_{max} = 0.275$. As a result, D_0 and k_0 can be calculated based on equations (2) and (3) by using the microstructural parameters (τ, ε and a) obtained from FIB tomography (see section 3.2) and $c_V \sim 2.3\times10^3$ mol/m^3, $c_O \sim 8.5\times10^4$ mol/m^3 estimated from the non-stoichiometry data for LSCF [31], and $f_{thermo} \sim 209$ for LSCF6428 at 800 °C from[32]. The results are plotted in Figure 2(b) and (c) together with k_0 and D_0 deduced from experiments including isotopic exchange, electronic conductivity and gravimetric relaxation on LSCF reported in the literature[5, 31, 33-37]. If chemical diffusion, D_{chem}, and chemical surface reaction rate, k_{chem}, were reported, they were converted to k_0 and D_0 assuming $D_{chem} = D_0 f_{thermo}\frac{c_O}{c_V}$ and $k_{chem} = k_0 f_{thermo}\frac{c_O}{c_V}$ [38].

For the Cr free reference sample, good agreement between the calculated and

10

literature data for D_0 is obtained and the values of k_0 are within the wider range of the literature data. The scatter in k_0 is likely due to large variations in the material surface conditions such as Sr surface segregation, which depends on many factors including thermal history, humidity, oxygen activity and electrode bias. Importantly, the results show clearly that Cr poisoning has led to a significant decrease in the values of both D_0 and k_0 by 1-2 orders of magnitude, explaining the degradation of the electrode conductivity. The activation energies of D_0 and k_0 are 2.23 ± 0.04 eV and 1.03 ± 0.08 eV respectively, and the average value is close to the activation energy obtained from the $R_{electrode}$. After poisoning, the activation energy of D_0 decreases slightly to 2.04 ± 0.03 eV while that of k_0 increases to 1.50 ± 0.06 eV.

3.2 Degradation of the cathode at the macro and micrometer level

XRD results reveal that the reference LSCF layer exhibits significant peaks that match best to a rhombohedral structure with $a = 5.4953$ Å and $c = 13.4125$ Å[39] (Figure S3), in agreement with literature reports for LSCF with similar stoichiometry ($La_{0.6}Sr_{0.4}Co_{0.2}Fe_{0.8}O_{3-\delta}$) at room temperature[40-41]. The principle structure remains the same after Cr impregnation. Additional peaks with low intensities arise in the Cr poisoned sample, which matches to a monoclinic $SrCrO_4$ phase.

At the micrometer scale, it can be seen that the morphology of the LSCF layer is similar for samples before and after Cr poisoning (Figure 3a), even though the Cr content in the poisoned sample was found to be ~ 2.7 at. % by SEM-EDX. However, distinct sub-micron to micron size Sr rich phases, as previously reported for LSCF poisoned for a prolonged period (as long as 380 hours) and/or with polarization[8, 42] were not identified in the current study, likely due to the different poisoning conditions used. Compared to other Cr poisoning experiments, which either directly contact high content

11

Cr alloys with the LSCF cathode or heat-treat samples in Cr oxide vapor, the concentration of Cr species available to react inside the LSCF cathode is expected to be higher due to the impregnation process, although the reaction time is much shorter.
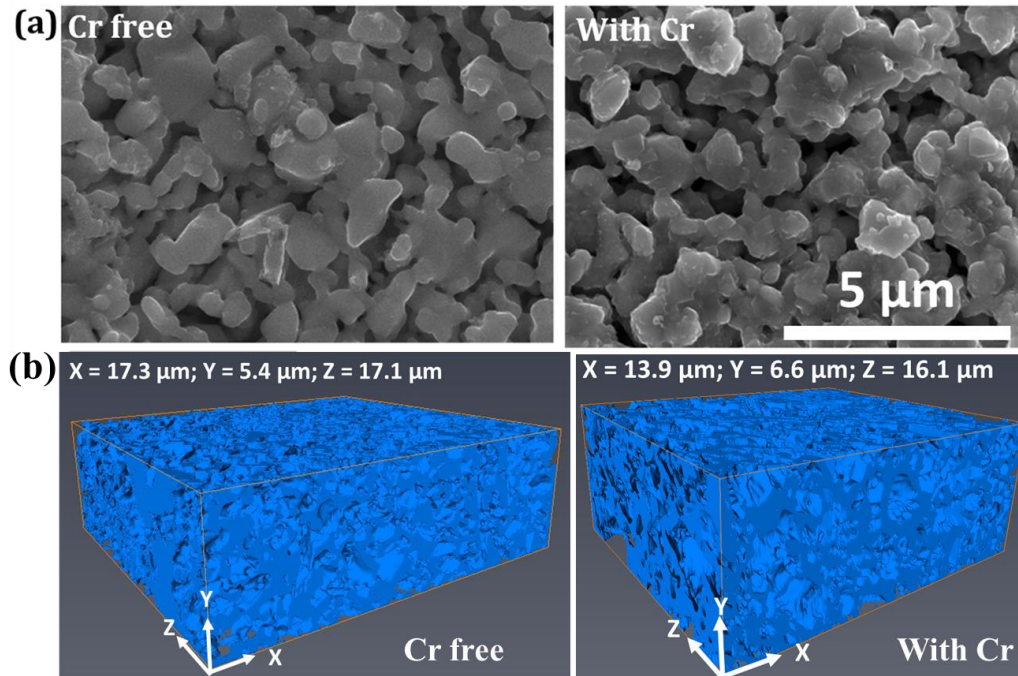

Figure 3 (a) SEM micrographs of the LSCF6428 cathode with and without Cr poisoning. (b) Sections from the reconstructed 3D volume of the pores in the reference (Cr free) and the Cr poisoned LSCF6428 electrodes. Dimensions of the volume are indicated. Direction X is perpendicular to the cathode/electrolyte interface.

More detailed characterization of the microstructure was obtained from FIB tomography. Snapshots of the reconstructed 3D volume of the reference and Cr poisoned LSCF electrodes are shown in Figure 3b, and Table 1 gives the quantitative microstructural parameters extracted from the analysis, including porosity, tortuosity factor of the solid phase, solid surface area per unit volume and mean pore sizes. The serial section results provide much better statistics than that of individual SEM micrographs further demonstrating that the difference between the reference and Cr poisoned sample at this micrometer level is very small.

Table 1 Microstructural parameters extracted from FIB-SEM tomography for the Cr free reference sample and the Cr poisoned sample.

	Reconstructed volume (μm^3)	Porosity (ε)	Solid phase surface area (a, m^{-1})	Tortuosity Factor (τ)
Cr free reference sample	1603	0.38±0.07	(3.17±0.51)×10^6	2.2±0.1
Cr poisoned sample	1846	0.37±0.08	(3.30±0.43)×10^6	2.2±0.1

3.3 Degradation of the cathodes at the nanoscale

3.3.1 Cr free sample

In order to separate any Cr effect from the rest of the processing conditions, samples without Cr impregnation were first studied as a reference. Figure 4a shows a scanning transmission electron microscopy (STEM) - annular dark field (ADF) image of a Cr-free sample with the elemental distribution. Co rich locations can be clearly seen, suggesting that Co has segregated out of the LSCF6428 grain as a result of the heat treatment at 900°C. Further EELS and EDX measurements (Figure S4) reveal that these Co rich particles also contain Fe and O and quantification with an experimental k factor approach (as described in the Experimental Section) indicates a composition of ~ $CoFeO_{3.5}$. Electron micro-diffraction analysis (Figure 4b) suggests that the phase adopts a $CoFe_2O_4$ spinel structure. A $CoFe_2O_4$ phase was reported previously for LSCF poisoned with Cr at cathodic polarization [17] and a micron size Co rich phase was reported after annealing at 800°C for 96 hours [42]. The current work confirms that Fe and Co segregation from LSCF into much smaller grains (~ <100 nm) happens within a very short period of time (5 hours at 900°C), which could not be identified with bulk XRD analysis due to the relatively low concentration of these segregants. Also, TEM analysis at the smaller scale reveals that although the particle has a spinel structure the composition deviates from the stoichiometric $CoFe_2O_4$ phase. It is possible that the $CoFeO_{3.5}$ is a transient phase before evolving into $CoFe_2O_4$ as a result of lower

13

availability of Co compared to Fe from LSCF. The previously reported $LaCoO_4$ phase after firing of $La_{0.6}Sr_{0.4}Co_{0.2}Fe_{0.8}O_3$ cathode at 1250 °C[16] was not observed in the current work, presumably due to the different firing conditions and stoichiometry of the material.
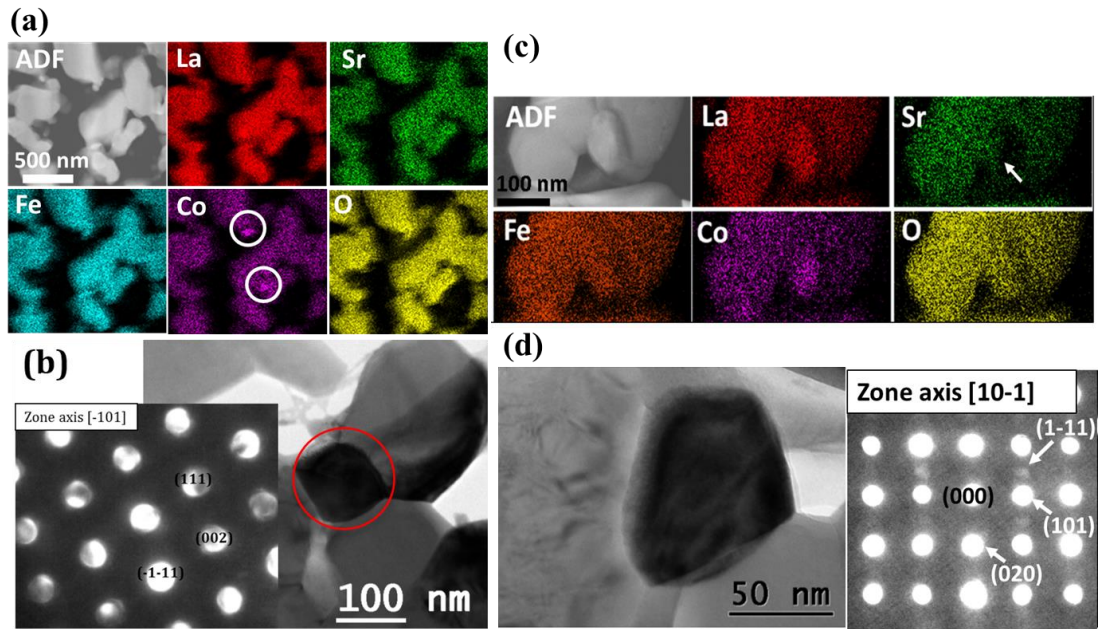

Figure 4 (a) and (c) Representative STEM ADF-EDX elemental maps of the Cr free reference sample. The intensity of the maps represents the net EDX counts after corrections for background and peak overlap. In (a), Co rich particles are circled in the map. (b) TEM bright field micrograph of a typical Fe-Co oxide particle with indexed electron micro-diffraction pattern confirming its spinel structure. In (c), a region deficient in Sr (arrowed) is shown. (d) The same Sr deficient particle with indexed electron micro-diffraction pattern confirming the structure has changed to a orthorhombic structure, different from the bulk rhombohedral phase.

Sr deficient regions, as shown in Figure 4c, were identified in the annealed sample. EDX quantification with experimental k factors reveals that the La/Sr ratio increased to ~5.8 compared to 1.5 as expected for LSCF6428. The observation suggests that Sr has exsolved from the perovskite lattice, in agreement with the reported surface Sr segregation on LSCF electrodes[43]. However, distinct Sr rich phases were not observed for samples after the short heat treatment as examined in the current work. Electron micro-diffraction data (Figure 4d) suggests that the Sr deficient phase can be best matched with an orthorhombic structure with $a= 5.6576$ Å, $b=7.8837$ Å and $c=5.4939$ Å[44], as expected for LSCF when the Sr content is decreased[45].

3.3.2   Cr poisoned sample

Representative STEM-EDX elemental mapping of the sample poisoned by Cr obtained is shown in Figure 5, where both the region inside the electrode and at the LSCF/CGO interface were examined. It is clear that the same Co-Fe spinel particles of ~ 100 nm or smaller were observed, but with a much higher density compared to the Cr free sample. Analysis of multiple elemental maps obtained from different areas of the samples suggests that the density increases from ~ $1/\mu m^2$ to $5/\mu m^2$. The Sr deficient and La enriched regions were again identified, with a higher frequency, and can be seen located preferentially close to the Cr rich areas (Figure 5b). A higher magnification STEM-EDX map of the Sr deficient area is shown in Figure 6a. EDX quantification suggests a similar La/Sr ratio of ~ 5.7 as found in the annealed sample without Cr. However, electron diffraction (Figure 6b) reveals that the Sr deficient region in this case retains the bulk rhombohedral structure and the adjacent region has a structure best matched to the cubic LSCF structure with $a = 3.9540$ Å[46].
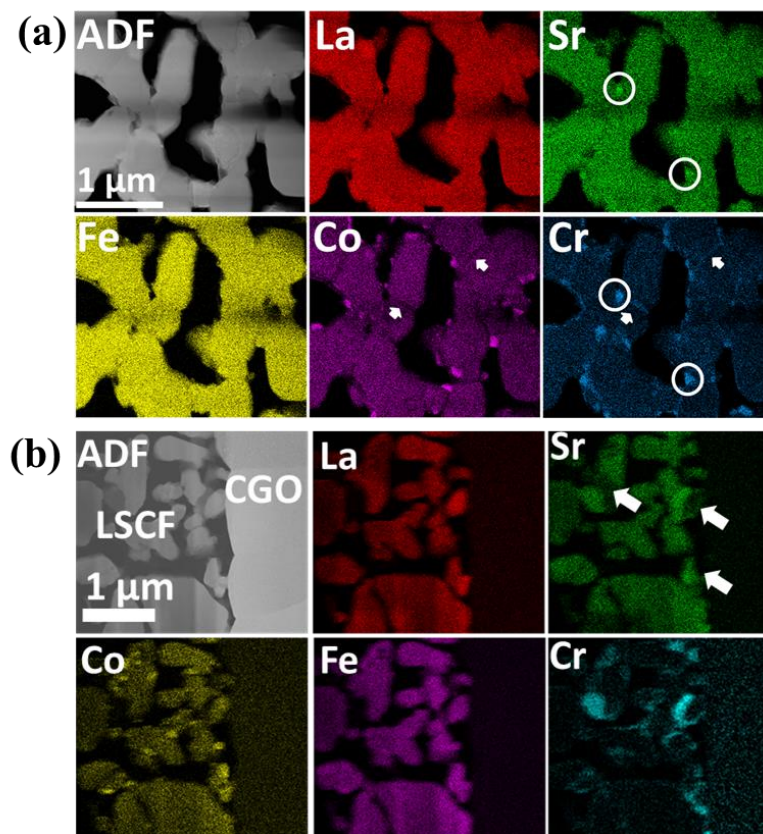
Figure 5 Representative STEM ADF-EDX elemental maps of the Cr poisoned sample obtained (a) from an area close to the LSCF6428 cathode surface and (b) from the LSCF6428/CGO interface. The intensity of the maps represents the net EDX counts after corrections for background and peak overlap. In (a) Some SrCrO$_4$ grains are indicated with circles. The grain boundaries enriched with Cr and deficient in Co are denoted with arrows. In (b), the La rich and Sr deficient regions are also highlighted with arrows.

Cr distribution is similar in both electrode and electrode/electrolyte interface regions, as expected from the current poisoning process. Cr rich locations can be seen predominantly at the pores and surface of the LSCF grains. These regions were identified by EDX as containing Sr, Cr and O. Electron micro-diffraction confirms that Sr and Cr rich particles have a structure matching the monoclinic SrCrO$_4$ as suggested by XRD. An example is shown in Figure S4. Formation of SrCrO$_4$ has been frequently reported in Cr poisoned LSCF[6, 17, 24], but the grain sizes observed in this work are mostly ~100-200 nm, much smaller than those found in other studies.
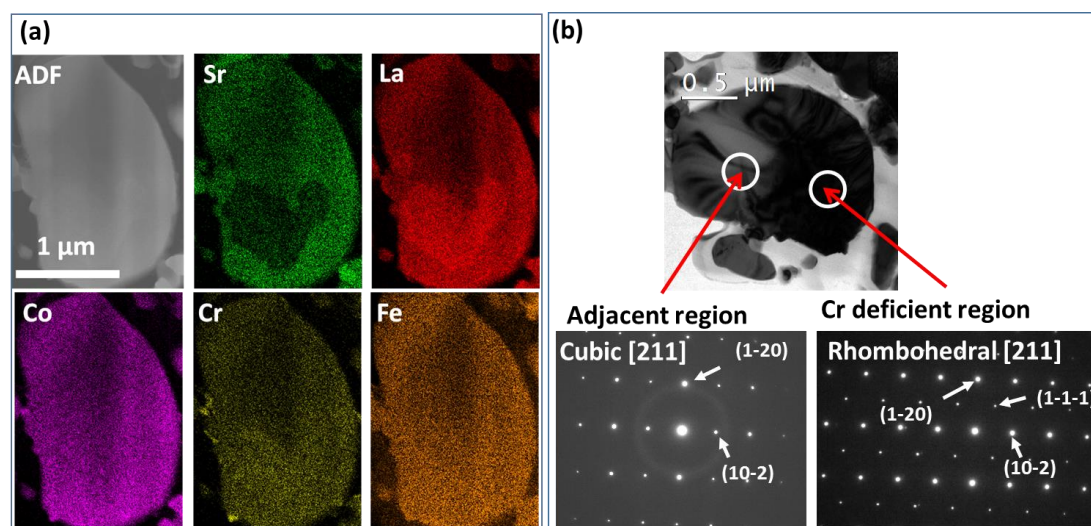

Figure 6 (a) Higher magnification STEM ADF-EDX mapping of La rich/Sr deficient region observed in the Cr poisoned LSCF6428 sample. The intensity of the elemental maps represents the net EDX counts after corrections for background and peak overlap. (b) Bright field micrograph of the same region together with the selected area diffraction pattern obtained from the La rich/Sr deficient region and an adjacent region.

Closer examination revealed for the first time that Cr segregates into LSCF grain boundaries (GBs) while Co is deficient at the grain boundary in the Cr poisoned LSCF electrode, as suggested in Figure 5a, and more clearly shown in the higher magnification STEM-EDX mapping of a LSCF grain boundary and the intensity line profile across the grain boundary (Figure 7a and b). Associated with the chemical

16

change, HRTEM of the same grain boundary reveals local areas of disorder at the grain boundary core although no amorphous glassy film was found to be present (Figure 7c). Although no data are available for Cr diffusion in LSCF, the Cr diffusion coefficients were reported to be approximately 6×10^{-21} m^2s^{-1} for lattice diffusion and 3×10^{-16} m^2s^{-1} for grain boundary diffusion in $La_{0.9}Sr_{0.1}FeO_{3-\delta}$ at 900°C [47]. Therefore, grain boundary segregation of Cr could potentially be facilitated by the fast diffusion along the grain boundary. It is noted that the results shown here represent changes at *true* grain boundaries across up to a few nanometers, which is different from the formation of Cr rich phases at much bigger open porosities between grains such as shown in previous studies [23].
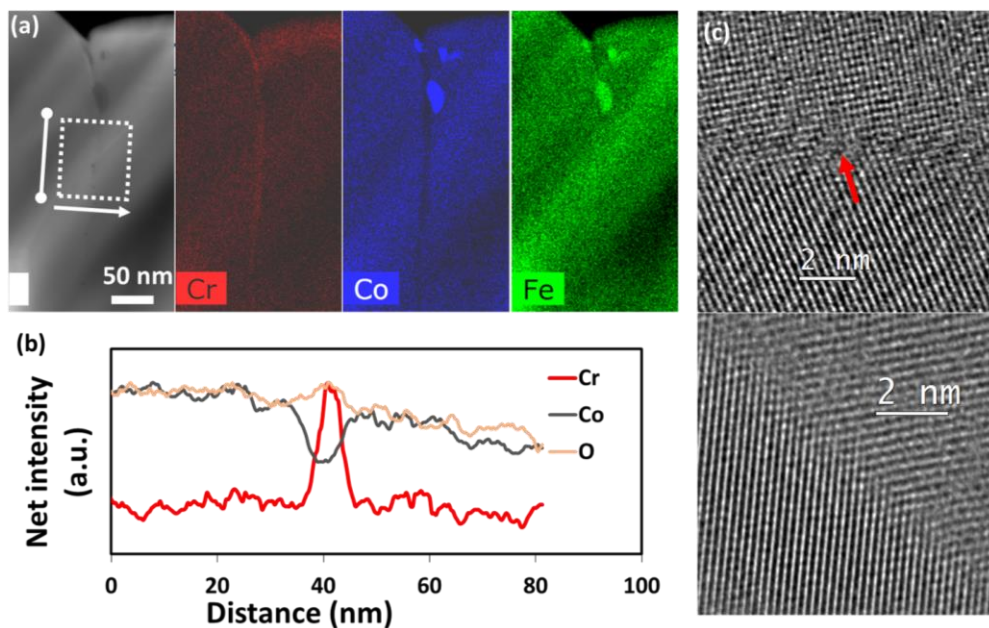

Figure 7 (a) STEM ADF-EDX elemental mapping of a LSCF6428 grain boundary in the Cr poisoned sample. The intensity of the elemental maps represents the net EDX counts after corrections for background and peak overlap. (b) The elemental net intensity change across the grain boundary as indicated in the image (a). To better show the segregation, the line profile was obtained by integrating along the direction parallel to the grain boundary, as indicated by the pointed line. The arrow shows the scan direction. (c) HRTEM images showing the same grain boundary structure, where no amorphous film can be identified, but a locally disordered area is observed (arrowed).

Apart from these Cr rich locations, EDX quantification also suggests the presence of Cr inside LSCF grains with a content of 1-3 at. %. The quantification also reveals that the higher the Cr content, the lower the Co and Fe content (Figure 8a). The Cr presence

was further confirmed by EELS analysis (Figure 8b), which is more reliable for low Cr content as there is no peak overlap as is the case with EDX. Again it can be seen that the Co and Fe $L_{2,3}$ edge intensity decreases with increasing Cr $L_{2,3}$ edge intensity in examined LSCF grains containing different levels of Cr. Applying experimental EELS k factors reveals that the Co/O atomic ratio decreases from the expected 0.07 for cation stoichiometric LSCF 6428 to 0.037 ± 0.004 and further to zero with increasing Cr level, and the Fe/O atomic ratio from an expected 0.27 to 0.24 ± 0.003 and 0.13 ± 0.002 at the same time. All of these results suggest that Cr has entered the perovskite B-site substituting Fe and Co, and Co can be completely depleted when the substituted Cr content is high.
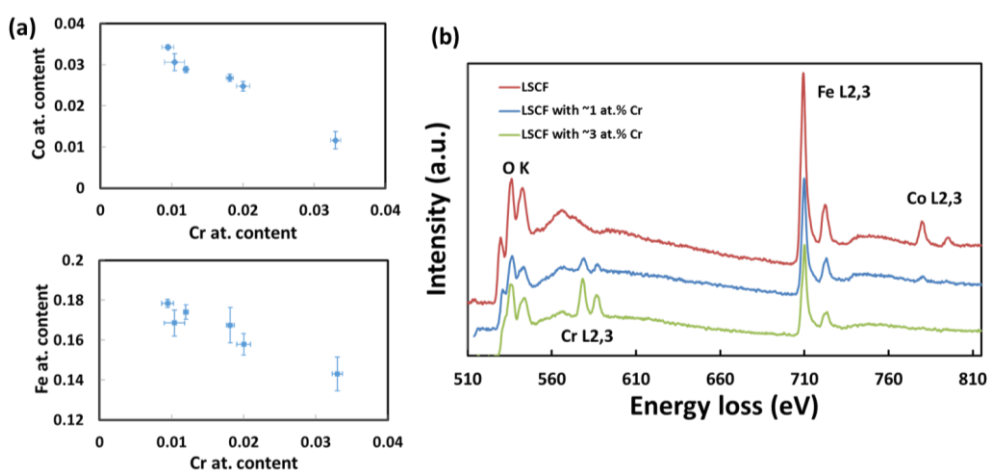

Figure 8 (a) Co and Fe atomic contents quantified by EDX using experimental k factor as a function of the Cr atomic content in different Cr substituted LSCF6428 grains. (b) EELS spectra obtained from Cr free LSCF6428 and Cr substituted LSCF6428.

The energy-loss near-edge structure (ELNES) of the O K-edge obtained from a Cr free LSCF sample, a Cr substituted area and the $SrCrO_4$ phase in a Cr poisoned sample is shown in Figure 9a. By probing the local density of the unoccupied states that is influenced by the chemical environment, ELNES can provide detailed structural and charge information of the investigated element. It can be seen that the O K-edge fine structure of the $SrCrO_4$ phase is distinctly different from that of LSCF, as expected from the different crystal structure of the two phases. The fine structure of LSCF

observed in this work is in good agreement with that reported for LSCF and similar perovskite materials[48-50]. According to the literature[51-52], the three main peaks marked as A, B and C can be attributed to excitations of the O 1s core states to unoccupied O 2p states hybridized with Fe and Co 3d states; with La 5d and Sr 4d states and with metal 4s and 4p states respectively. The region up to 30–50 eV above the threshold relates to the multiple scattering of the excited electrons by neighbouring oxygen atoms[53]. The fact that these features remain very similar in Cr substituted LSCF compared to that of Cr free LSCF further supports Cr incorporation into the original perovskite structure without significant changes to the parent crystal structure. Meanwhile, a reduction in the intensity of peak A was observed for LSCF substituted with a higher content of Cr (~ 3 at.%). As this peak is related to the unoccupied O 2p states hybridized with Fe and Co 3d states, the reduced intensity can be attributed to a reduction in the transition metal valence leading to filling of the hybridized states, as found for Ti in $Nd_{1-x}TiO_3$ [54] and in $La_xSr_{1-x}TiO_3$ [55].
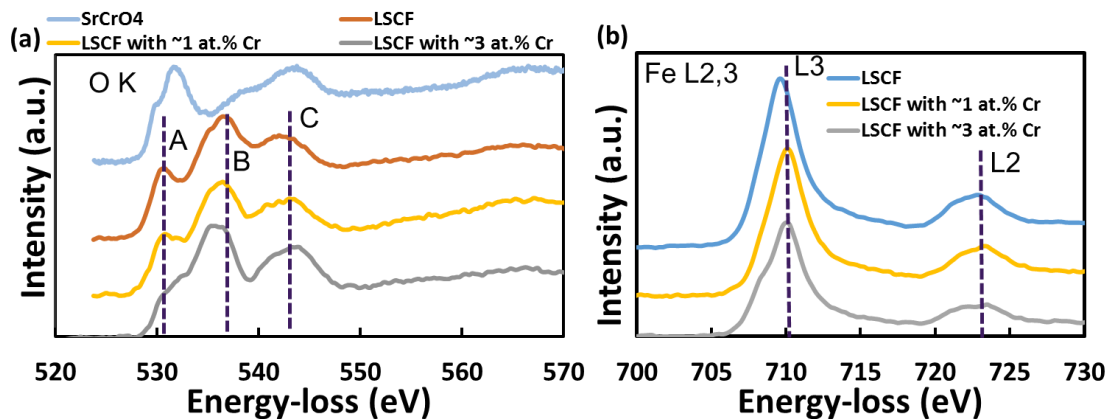

Figure 9 EELS ELNES of (a) O K and (b) Fe $L_{2,3}$ edges for Cr free and substituted LSCF. In (a), the data obtained from the $SrCrO_4$ phase is also included for comparison.

The valence state for Fe was further examined with the Fe L_2 and L_3 white lines (Figure 9b). Subtle changes can be noticed in LSCF with the higher level of Cr substitution (~ 3 at.%). The appearance of the pre-peak at the L_3 line and minor splitting of the L_2 line are finger prints for a higher portion of Fe^{3+} compared to Fe^{4+} or Fe^{2+} [25]. Further, the

L_3/L_2 white-line ratio was extracted quantitatively using the approach described in the experimental section. The ratio increased from 4.07±0.16 for as-sintered LSCF, to 4.65 ± 0.09 for the Cr free reference LSCF, and to 5.16 ± 0.12 for LSCF grains containing ~3 at.% Cr. It is well known that the L_3/L_2 ratio varies as a function of the valence state and reaches the maximum at 3+ for Fe [25]. Considering that Fe is expected to exhibit a mixed 3+ and 4+ valence with the average of ~3.4+ in LSCF [56], an increase in the white line ratio suggests that the Fe average valence decreases upon thermal treatment of the sample and further with Cr substitution. The reduction after heat treatment is likely due to the Sr depletion from the A-site, while the further reduction might be related to the presence of Cr^{6+} in the Cr containing perovskite, e.g. $LaCrO_3$, $La_{1-x}Sr_xFe_{0.8}Cr_{0.2}O_{3-y}$ [57] and $La_{0.75}Sr_{0.25}Cr_{0.5}Fe_{0.5}O_{3-\delta}$ (LSCrF) [58].

Cr substitution into the LSCF lattice has been predicted to be a favorable process by thermodynamic calculations[59], but no experimental evidence has been previously reported for Cr substitution of LSCF cathodes during the poisoning process. It was suspected that this is because the process is kinetically very slow. At the micrometer level, a previous study suggested that when poisoned with Cr containing alloys, Cr substitution happpened for $(La_{0.8}Sr_{0.2})_{0.99}FeO_3$ (LSF) while not for LSCF[12]. The current work confirms that Cr substitution occurs after reacting with Cr for a short time period in current poisoning conditions, but can only be detected at high resolution as the level of substitution is low and inhomogeneous. The Cr substitution in the B-site might act as a driving force for Fe and Co precipitation and explains the enhanced Fe-Co segregation in Cr poisoned samples.

3.4 Role of change of micron/nano scale structure and chemistry in LSCF degradation

It is confirmed in the current work that Cr poisoning has a significant poisoning effect on LSCF6428 by degrading both the oxygen surface reaction rate k_0 and oxygen diffusivity D_0 of the material. From bulk characterization of the Cr poisoned LSCF using techniques such as XRD, only the formation of $SrCrO_4$ phase has been suggested, however the size of this phase is too small to be detected by SEM. Furthermore, FIB tomography reveals an almost identical microstructure for both the Cr free and Cr poisoned samples. Therefore, under the conditions used in this study, Cr poisoning of the LSCF cathode induces negligible change of structure and chemistry at the micron scale and plays little role in the material property degradation.

Although Sr deficient regions and formation of the Fe-Co oxide was already identified after the 5-hour heat treatment without Cr poisoning, the combined effect on the total polarization resistance of the electrode after 5 hours is negligible (Figure S6). This may be due to either the subtle nature of the changes or the possible enhancing effect of Fe-Co oxides counteracting the detrimental Sr deficiency. It was suggested that the formation of this Fe-Co spinel phase reduced the LSCF degradation from Cr poisoning [17], and also that infiltration of Co_2O_3 nanoparticles into LSM improves the cathode performance [60].

The formation of nanometer size Cr rich phases, mainly the $SrCrO_4$ with low conductivity (1.8×10^{-4} Ohm^{-1} cm^{-1} at 800 ºC [61]), at the electrode surface explains the increase in the ohmic resistance consistently observed in the Cr poisoned sample (Figure 1). This phase is also expected to reduce the number of active surface sites for oxygen exchange, and contributes to the observed reduction in the oxygen surface exchange rate k_0. The precipitation of Fe-Co spinel, which is greatly enhanced by Cr poisoning, may have a positive effect on k_0, as discussed earlier. The fact that overall

the surface exchange rate was reduced indicates that this possible positive effect is smaller than other negative effects caused by Cr poisoning.

The change of bulk and surface stoichiometry is suggested both as a result of thermal treatment and Cr poisoning. The presence of La rich/Sr deficient grains, sometimes with changes to the crystal structure (from rhombohedral to orthorhombic, Figure 4d), or induced structural change of adjacent grains (from rhombohedral to cubic, Figure 6b), were seen after annealing and Cr poisoning. This could degrade both the surface exchange properties and oxygen diffusion coefficient as a reduction in the oxygen vacancy concentration is expected upon depletion of the Sr dopant in LSCF.

LSCF stoichiometry was also altered by the substitution of Cr at the B-sites leading to reduced amounts of Fe and Co. It was found that Co is almost completely depleted at ~3 at.% of Cr substitution. It has been shown that oxygen vacancies would form preferentially around Co in LSCF [56], therefore a decrease in oxygen vacancy concentration is expected upon Co depletion. The conductivity of a Cr containing perovskite has been reported to be lower than that of LSCF6428 (~25 S cm^{-1} at 500°C for $La_{0.6}Sr_{0.4}CrO_3$ [62] and 21.88 S cm^{-1} at 800°C for $La_{0.8}Sr_{0.2}Cr_{0.5}Fe_{0.5}O_{3-\delta}$ [63] compared to ~ 50 S cm^{-1} at 500°C for LSCF 6428[64]). Takeda et al. also reported that the catalytic activity of perovskite electrodes for oxygen reduction decreases in the following order: $La_{1-x}Sr_xCoO_{3-\delta}$, $La_{1-x}Sr_xMnO_{3-\delta}$, $La_{1-x}Sr_xFeO_{3-\delta}$ and $La_{0.7}Sr_{0.3}CrO_{3-\delta}$ [65]. All of these facts can contribute to the reduced D_0 and k_0 for the Cr poisoned sample. The activation energy of the surface exchange for LSCF6428 was reported to be only half that of $(La_{0.6}Sr_{0.4})FeO_{3-\delta}$ [66] and that of a Cr containing perovskite such as $La_{0.2}Sr_{0.8}Cr_{0.2}Fe_{0.8}O_{3-\delta}$ appears to be low as well [67-68]. Therefore, the slight increase of the activation energy for k_0 (Figure 2c) is probably due to the much-reduced Co content and Cr substitution

in the Cr poisoned LSCF sample. The Sr solution energy has been calculated to be lower for $LaCo_{0.8}Fe_{0.2}O_3$ than that for $LaCo_{0.8}Cr_{0.2}O_3$, leading to a more ready dissolution of Sr in $LaCo_{0.8}Fe_{0.2}O_3$ [69]. The Cr substitution and resulted reduction in the Fe content in LSCF may have contributed to the Sr exsolution in Cr poisoned sample.

The current work also suggests a decrease in Fe valence upon Cr substitution. On one hand, this may be beneficial as it has been suggested that lower B-site cation valence will facilitate oxygen ion vacancy hopping resulting from reduced interaction between B-cations and oxygen ions; on the other hand, it could hinder the oxygen vacancy formation as the required reduction process is more difficult with the lower valence state. It was not possible to analyze the change of Co valence using the white line ratio method, due to the very low intensity of the Co edge in the Cr substituted regions, but similar reduction in Co valence may be expected.

Lastly, the significant change of grain boundary chemistry is clearly shown in this work. Although no grain boundary diffusion data is available for Cr poisoned LSCF, our analysis shows that the grain boundary is enriched in Cr and deficient in Co, which suggests a composition similar to LSCrF. Due to the lower oxygen conductivity of the LSCrF phase, an increase in the grain boundary resistance is expected. Although the ALS theory used in this work for extracting D_0 assumes that oxygen diffusion is homogeneous and in the bulk, the apparent oxygen diffusion coefficient will be reduced if the oxygen has to cross more resistive grain boundaries to reach the electrolyte in Cr-poisoned LSCF. It is noted that in the present study Cr grain boundary segregation (and Co deficiency) was more frequently found than Cr substitution in LSCF, which was expected as a result of faster grain boundary diffusion than bulk diffusion. Therefore, grain boundary segregation of Cr might have played a major role in reducing the

apparent oxygen diffusivity.

Although one approach to mitigate Cr poisoning is to develop interconnect coatings that can reduce Cr evaporation, it has been shown to be very difficult to eliminate the Cr evaporation completely[70] and a very small amount of Cr contamination (0.1%) can significantly poison the electrode[5]. The development of a more Cr poisoning resistant electrode material is therefore necessary, which requires the identification and understanding of all effective poisoning mechanisms. The new mechanisms revealed in the current work can provide a basis for future studies to understand the contribution from each of the above discussed nanoscale changes to the cathode degradation. For example, a reduction of Cr segregation at the grain boundaries may significantly increase the poisoning resistance, which could be achieved by doping suitable dopants that preferentially segregate to grain boundaries forming phases with high conductivity.

4   Conclusions

Cr poisoning was carried out by impregnating $Cr(NO_3)_3.9H_2O$ solution into porous LSCF6428 cathodes followed by heat treatment at 900°C for 5 hours. The poisoning mechanisms were studied by parallel EIS analysis and investigation of the intrinsic reactivity of Cr species with LSCF at the micro- to nano-scale using a combination of FIB-SEM and multiple TEM techniques. The Cr free samples undergoing the same processing and annealing conditions were first characterized to isolate the effects of introducing Cr. It was found that strong Co-Fe co-segregation, in the form of Co-Fe spinel oxides, occurs after annealing for 5 hours and La rich/Sr depletion regions were also identified; however, no Sr rich phases could be detected. Under current poisoning conditions, an overall Cr content of ~ 2.7 at.% was obtained in poisoned sample, which corresponds to a reduction of both k_0 and D_0 by 1-2 orders of magnitude measured by

EIS. At this significant level of poisoning, while detailed FIB-SEM tomography reveals no significant structural change and Cr rich phases at the micrometer scale, Cr incorporation was clearly identified at the nanometer level and below. We showed that the quality of our high-resolution analysis enabled us to achieve the level of details that were not available before. The $SrCrO_4$ phase formed after Cr poisoning with the current condition has a significantly smaller size (< 100 nm) than what was previously reported. For the first time, Cr substitution into the perovskite structure predicted by thermodynamic calculations was confirmed experimentally, which was associated with a decrease in the original B-site Fe and Co contents and in the Fe valence. The Fe-Co spinel formation was greatly enhanced after Cr poisoning, likely to be a result of the Cr substitution. We also showed the first experimental evidence of Cr segregation to the LSCF grain boundaries associated with Co deficiency. The methodology developed and the new degradation mechanisms identified in this work provides the essential insight and guidance for future work studying SOFC degradation, which will be directed towards poisoning of cells under more realistic operation and poisoning conditions for the development of more poisoning resistant SOFC electrode materials.

Supporting Information. Electrode preparation; Cr poisoning of LSCF cathodes of the symmetric cell; FIB-SEM tomography; Measurement of experimental k factors for EDX and EELS; Analysis of Fe valence; XRD characterization of the LSCF6428 cathode; EELS and EDX spectrum from typical Fe-Co spinel particles; Bright field image of typical SrCrO4 grain with indexed micro-diffraction pattern and STEM-EDX spectrum; Change of the total polarization resistance for the LSCF electrode as a function of heat treatment time at 900°C; Fitted impedance parameters measured at 550 – 780 ˚C.

References

1.   Aguadero, A.; Fawcett, L.; Taub, S.; Woolley, R.; Wu, K. T.; Xu, N.; Kilner, J. A.; Skinner, S. J. Materials Development for Intermediate-temperature Solid Oxide Electrochemical Devices. *J. Mater. Sci.* **2012,** *47* (9), 3925-3948.

2.   Thomann, O.; Pihlatie, M.; Schuler, J. A.; Himanen, O.; Kiviaho, J. Method for Measuring Chromium Evaporation from SOFC Balance-of-Plant Components. *Electrochem. Solid-State Lett.* **2012,** *15* (3), B35-B37.

3.   Tucker, M. C.; Kurokawa, H.; Jacobson, C. P.; De Jonghe, L. C.; Visco, S. J. A Fundamental Study of Chromium Deposition on Solid Oxide Fuel Cell Cathode Materials. *J. Power Sources* **2006,** *160* (1), 130-138.

4.   Jiang, S. P.; Chen, X. B. Chromium Deposition and Poisoning of Cathodes of Solid Oxide Fuel Cells - A review. *Int. J. Hydrogen Energy* **2014,** *39* (1), 505-531.

5.   Lee, S. N.; Atkinson, A.; Kilner, J. A., Effect of Chromium On $La_{0.6}Sr_{0.4}Co_{0.2}Fe_{0.8}O_{3-delta}$ Solid Oxide Fuel Cell Cathodes. *J. Electrochem. Soc.* **2013,** *160* (6), F629-F635.

6.   Wei, B.; Chen, K.; Wang, C. C.; Lü, Z.; Jiang, S. P. Cr Deposition on Porous $La_{0.6}Sr_{0.4}Co_{0.2}Fe_{0.8}O_{3-\delta}$ Electrodes of Solid Oxide Cells Under Open Circuit Condition. *Solid State Ionics* **2015,** *281*, 29-37.

7.   Esquirol, A.; Brandon, N. P.; Kilner, J. A.; Mogensen, M. Electrochemical Characterization of $La_{0.6}Sr_{0.4}Co_{0.2}Fe_{0.8}O_3$ Cathodes for Intermediate-Temperature SOFCs. *J. Electrochem. Soc.* **2004,** *151* (11), A1847.

8.   Jiang, S. P.; Zhang, S.; Zhen, Y. D. Deposition of Cr Species at $(La,Sr)(Co,Fe)O_3$ Cathodes of Solid Oxide Fuel Cells. *J. Electrochem. Soc.* **2006,** *153* (1), A127.

9.   Jiang, S. P.; Zhang, J. P.; Zheng, X. G. A Comparative Investigation of Chromium Deposition at Air Electrodes of Solid Oxide Fuel Cells. *J. Eur. Ceram. Soc.* **2002,** *22* (3), 361-373.

10.   Badwal, S. P. S.; Deller, R.; Foger, K.; Ramprakash, Y.; Zhang, J. P. Interaction Between Chromia Forming Alloy Interconnects and Air Electrode of Solid Oxide Fuel Cells. *Solid State Ionics* **1997,** *99* (3-4), 297-310.

11.   Hilpert, K.; Das, D.; Miller, M.; Peck, D. H.; Weiß, R. Chromium Vapor Species over Solid Oxide Fuel Cell Interconnect Materials and Their Potential for Degradation Processes. *J. Electrochem. Soc.* **1996,** *143* (11), 3642-3647.

12.   Simner, S. P.; Anderson, M. D.; Xia, G.-G.; Yang, Z.; Pederson, L. R.; Stevenson, J. W. SOFC Performance with Fe-Cr-Mn Alloy Interconnect. *J. Electrochem. Soc.* **2005,** *152* (4), A740-A745.

13.   Fujita, K.; Hashimoto, T.; Ogasawara, K.; Kameda, H.; Matsuzaki, Y.; Sakurai, T. Relationship Between Electrochemical Properties of SOFC Cathode and Composition of Oxide Layer Formed on Metallic Interconnects. *J. Power Sources* **2004,** *131* (1–2), 270-277.

14.   Matsuzaki, Y.; Yasuda, I. Dependence of SOFC Cathode Degradation by Chromium-containing Alloy on Compositions of Electrodes and Electrolytes. *J. Electrochem. Soc.* **2001,** *148* (2), A126-A131.

15.   Kim, J. Y.; Sprenkle, V. L.; Canfield, N. L.; Meinhardt, K. D.; Chick, L. A. Effects of Chrome Contamination on the Performance of La0.6Sr0.4Co0.2Fe0.8O3 Cathode Used in Solid Oxide Fuel Cells. *J. Electrochem. Soc.* **2006,** *153* (5), A880-A886.

16.   Kiebach, R.; Zhang, W.-W.; Zhang, W.; Chen, M.; Norrman, K.; Wang, H.-J.; Bowen, J. R.; Barfod, R.; Hendriksen, P. V. Stability of La$_{0.6}$Sr$_{0.4}$Co$_{0.2}$Fe$_{0.8}$O3/Ce$_{0.9}$Gd$_{0.1}$O$_2$ Cathodes During Sintering and Solid Oxide Fuel Cell Operation. *J. Power Sources* **2015,** *283*, 151-161.

17.   Cho, D.-H.; Kishimoto, H.; Yamaji, K.; Brito, M. E.; Develos- Bagarinao, K.; Nishi, M.; Shimonosono, T.; Wang, F.; Yokokawa, H.; Horita, T. Evaluation of the Cathode Performance and the Distribution of Deposited Cr Species in the LSCF6428 Cathod. *ECS Trans.* **2013,** *57* (1), 1865-1872.

18.   Konysheva, E.; Penkalla, H.; Wessel, E.; Mertens, J.; Seeling, U.; Singheiser, L.; Hilpert, K. Chromium Poisoning of Perovskite Cathodes by the ODS Alloy Cr5Fe1Y2O3 and the High Chromium Ferritic Steel Crofer22APU. *J. Electrochem. Soc.* **2006,** *153* (4), A765-A773.

19.   Sharma, V. I.; Yildiz, B. Degradation Mechanism in La0.8Sr0.2CoO3 as Contact Layer on the Solid Oxide Electrolysis Cell Anode. *J. Electrochem. Soc.* **2010,** *157* (3), B441-B448.

20.   Schuler, J. A.; Yokokawa, H.; Calderone, C. F.; Jeangros, Q.; Wuillemin, Z.; Hessler-Wyser, A.; Van Herle, J. Combined Cr and S Poisoning in Solid Oxide Fuel Cell Cathodes. *J. Power Sources* **2012,** *201*, 112-120.

21.   Stodolny, M. K.; Boukamp, B. A.; Blank, D. H. A.; van Berkel, F. P. F. Cr-Poisoning of a LaNi$_{0.6}$Fe$_{0.4}$O$_3$ Cathode Under Current Load. *J. Power Sources* **2012,** *209*, 120-129.

22.   Ni, N.; Skinner, S., Combined Cr and Mo Poisoning of (La,Sr)(Co,Fe)O$_{3-\delta}$ Solid Oxide Fuel Cell Cathodes at the Nanoscale. *Solid State Ionics* **2016**, *288*, 28-31.

23.   Park, E.; Taniguchi, S.; Daio, T.; Chou, J.-T.; Sasaki, K. Influence of Cathode Polarization on the Chromium Deposition Near the Cathode/Electrolyte Interface of SOFC. *Int. J. Hydrogen Energy* **2014,** *39* (3), 1463-1475.

24.   Lu, K.; Shen, F. Effect of Stoichiometry on (La$_{0.6}$Sr$_{0.4}$)xCo$_{0.2}$Fe$_{0.8}$O$_3$ Cathode Evolution inSolid oxide Fuel Cells. *J. Power Sources* **2014,** *267*, 421-429.

25.   Tan, H.; Verbeeck, J.; Abakumov, A.; Van Tendeloo, G. Oxidation State and Chemical Shift Investigation in Transition Metal Oxides by EELS. *Ultramicroscopy* **2012,** *116*, 24-33.

26.   van Aken, P. A.; Liebscher, B.; Styrsa, V. J. Quantitative Determination of Iron Oxidation States in Minerals using Fe L 2,3 -edge Electron Energy-Loss Near-Edge Structure Spectroscopy. *Phys. Chem. Miner.* **1998,** *25* (5), 323-327.

27.   Nielsen, J.; Jacobsen, T.; Wandel, M., Impedance of porous IT-SOFC LSCF:CGO composite cathodes. *Electrochimica Acta* **2011,** *56* (23), 7963-7974.

28.   Sayers, R.; Rieu, M.; Lenormand, P.; Ansart, F.; Kilner, J. A.; Skinner, S. J. Development of Lanthanum Nickelate as a Cathode for Use in Intermediate Temperature Solid Oxide Fuel Cells. *Solid State Ionics* **2011,** *192* (1), 531-534.

29.   Zhao, K.; Xu, Q.; Huang, D.-P.; Chen, W.; Chen, M.; Kim, B.-H. Microstructure and Electrochemical Properties of Porous La$_2$NiO$_{4+\delta}$ Electrode Screen-printed on Ce$_{0.8}$Sm$_{0.2}$O$_{1.9}$ Electrolyte. *J Solid State Electrochem* **2012,** *16* (1), 9-16.

30.   Adler, S. B.; Lane, J. A.; Steele, B. C. H. Electrode Kinetics of Porous Mixed-Conducting Oxygen Electrodes. *J. Electrochem. Soc.* **1996,** *143* (11), 3554-3564.

31.   Bouwmeester, H. J. M.; Den Otter, M. W.; Boukamp, B. A. Oxygen Transport in La$_{0.6}$Sr$_{0.4}$Co$_{1-y}$Fe$_y$O$_{3-\delta}$. *J Solid State Electrochem* **2004,** *8* (9), 599-605.

32.   Lane, J. A.; Benson, S. J.; Waller, D.; Kilner, J. A. Oxygen Transport in La$_{0.6}$Sr$_{0.4}$Co$_{0.2}$Fe$_{0.8}$O$_{3-\delta}$. *Solid State Ionics* **1999,** *121* (1–4), 201-208.

33.   Katsuki, M.; Wang, S.; Dokiya, M.; Hashimoto, T. High Temperature Properties of La$_{0.6}$Sr$_{0.4}$Co$_{0.8}$Fe$_{0.2}$O$_{3-\delta}$ Oxygen Nonstoichiometry and Chemical Diffusion Constant. *Solid State Ionics* **2003,** *156* (3–4), 453-461.

34.   Ried, P.; Bucher, E.; Preis, W.; Sitte, W.; Holtappels, P. Characterisation of La$_{0.6}$Sr$_{0.4}$Co$_{0.8}$Fe$_{0.2}$O$_{3-d}$ and Ba$_{0.5}$Sr$_{0.5}$Co$_{0.8}$Fe$_{0.2}$O$_{3-d}$ as Cathode Materials for the Application in Intermediate Temperature Fuel Cells. *ECS Trans.* **2007,** *7* (1), 1217-1224.

35.   Lane, J. A.; Kilner, J. A. Measuring Oxygen Diffusion and Oxygen Surface Exchange by Conductivity Relaxation. *Solid State Ionics* **2000,** *136–137*, 997-1001.

36.   Bucher, E.; Sitte, W.; Klauser, F.; Bertel, E. Oxygen Exchange Kinetics of La$_{0.58}$Sr$_{0.4}$Co$_{0.2}$Fe$_{0.8}$O$_3$ at 600 °C in Dry and Humid Atmospheres. *Solid State Ionics* **2011,** *191* (1), 61-67.

37.   Benson, S. J.; Chater, R. J.; Kilner, J. A. In *Oxygen Diffusion and Surface Exchange in the Mixed Conducting Perovskite La$_{0.6}$Sr$_{0.4}$Fe$_{0.8}$Co$_{0.2}$O$_{3-\Delta}$,* Pennington, NJ, T.A. Ramanarayanan; W.L.Worrell; H.L. Tuller; M. Mogensen; A. Khandkar, Eds. 1st ed.; Electrochemical Society: Pennington, NJ, **1997**; pp 596-609.

38.   Mauvy, F.; Bassat, J. M.; Boehm, E.; Dordor, P.; Grenier, J. C.; Loup, J. P. Chemical Oxygen Diffusion Coefficient Measurement by Conductivity Relaxation - Correlation Between Tracer Diffusion Coefficient and Chemical Diffusion Coefficient. *J. Eur. Ceram. Soc.* **2004,** *24* (6), 1265-1269.

39.   Cesário, M. R.; Macedo, D. A.; Martinelli, A. E.; Nascimento, R. M.; Barros, B. S.; Melo, D. M. A. Synthesis, Structure and Electrochemical Performance of Cobaltite-Based Composite Cathodes for IT-SOFC. *Cryst. Res. Technol.* **2012,** *47* (7), 723-730.

40.   Waller, D.; Lane, J. A.; Kilner, J. A.; Steele, B. C. H. The Structure of and Eeaction of A-site Deficient La$_{0.6}$Sr$_{0.4-x}$Co$_{0.2}$Fe$_{0.8}$O$_{3-\delta}$ Perovskites. *Mater. Lett.* **1996,** *27* (4–5), 225-228.

41.   Huang, B. X.; Malzbender, J.; Steinbrech, R. W.; Singheiser, L. Mechanical Properties of La$_{0.58}$Sr$_{0.4}$Co$_{0.2}$Fe$_{0.8}$O$_{3-\delta}$ Membranes. *Solid State Ionics* **2009,** *180* (2–3), 241-245.

42.   Zhao, L.; Drennan, J.; Kong, C.; Amarasinghe, S.; Jiang, S. P., Surface Segregation and Chromium Deposition and Poisoning on La$_{0.6}$Sr$_{0.4}$Co$_{0.2}$Fe$_{0.8}$O$_{3-\delta}$ Cathodes of Solid Oxide Fuel Cells. *ECS Trans.* **2013,** *57* (1), 599-604.

43.   Druce, J.; Tellez, H.; Burriel, M.; Sharp, M. D.; Fawcett, L. J.; Cook, S. N.; McPhail, D. S.; Ishihara, T.; Brongersma, H. H.; Kilner, J. A. Surface Termination and Subsurface Restructuring of Perovskite-based Solid Oxide Electrode Materials. *Energy Environ. Sci.* **2014,** *7* (11), 3593-3599.

44.   Arul Raj, I.; Nesaraj, A. S.; Kumar, M.; Tietz, F.; Buchkremer, H. P.; Stöver, D. On the Suitability of La$_{0.6}$Sr$_{0.4}$Co$_{0.2}$Fe$_{0.8}$O$_3$ Cathode for the Intermediate Temperature Solid Oxide Fuel Cell (ITSOFC). *J. New Mater. Electrochem. Syst.* **2004,** *7*, 145 - 151.

45.   Tai, L. W.; Nasrallah, M. M.; Anderson, H. U.; Sparlin, D. M.; Sehlin, S. R. Structure and Electrical Properties of La$_{1-x}$Sr$_x$Co$_{1-y}$Fe$_y$O$_3$. Part 2. The system La$_{1-x}$Sr$_x$Co$_{0.2}$Fe$_{0.8}$O$_3$. *Solid State Ionics* **1995,** *76* (3–4), 273-283.

46.   Yashima, M.; Kamioka, T. Neutron Diffraction Study of the Perovskite-type Lanthanum Cobaltite La$_{0.6}$Sr$_{0.4}$Co$_{0.8}$Fe$_{0.2}$O$_{3-\delta}$ at 1260 °C and 394 °C. *Solid State Ionics* **2008,** *178* (39–40), 1939-1943.

47.	Wærnhus, I.; Sakai, N.; Yokokawa, H.; Grande, T.; Einarsrud, M.-A.; Wiik, K. Cation Diffusion in $La_{1-x}Sr_xFeO_{3-\delta}$, x = 0 and 0.1 Measured by SIMS. *Solid State Ionics* **2007,** *178* (13–14), 907-914.

48.	Ravkina, O.; Klande, T.; Feldhoff, A. Investigation of Carbonates in Oxygen-transporting Membrane Ceramics. *J. Membr. Sci.* **2015,** *480*, 31-38.

49.	Arnold, M.; Xu, Q.; Tichelaar, F. D.; Feldhoff, A. Local Charge Disproportion in a High-Performance Perovskite. *Chem. Mater.* **2009,** *21* (4), 635-640.

50.	Klie, R. F.; Browning, N. D. Atomic Scale Characterization of Vacancy Ordering in Oxygen Conducting Membranes. *Microsc. Microanal.* **2002,** *8* (06), 475-486.

51.	Abbate, M.; de Groot, F. M. F.; Fuggle, J. C.; Fujimori, A.; Strebel, O.; Lopez, F.; Domke, M.; Kaindl, G.; Sawatzky, G. A.; Takano, M.; Takeda, Y.; Eisaki, H.; Uchida, S. Controlled-valence Properties of $La_{1-x}Sr_xFeO_3$ and $La_{1-x}Sr_xMnO_3$ Studied by Soft-x-ray Absorption Spectroscopy. *Phys. Rev. B* **1992,** *46* (8), 4511-4519.

52.	Verbeeck, J.; Lebedev, O. I.; Van Tendeloo, G.; Silcox, J.; Mercey, B.; Hervieu, M.; Haghiri-Gosnet, A. M. Electron Energy-loss Spectroscopy Study of a $(LaMnO_3)_8(SrMnO_3)_4$ Heterostructure. *Appl. Phys. Lett.* **2001,** *79* (13), 2037-2039.

53.	Murakami, Y.; Shindo, D.; Kikuchi, M.; Zuo, J. M.; Spence, J. C. H. Resonance Effect in ELNES from Perovskite-type Manganites $BiMnO_3$ and $LaMnO_3$. *J. Electron Microsc.* **2002,** *51* (2), 99-104.

54.	Sefat, A. S.; Amow, G.; Wu, M.-Y.; Botton, G. A.; Greedan, J. E. High-resolution EELS Study of the Vacancy-doped Metal/Insulator System, $Nd_{1-x}TiO_3$, x=0 to 0.33. *J. Solid State Chem.* **2005,** *178* (4), 1008-1016.

55.	Fujimori, A.; Hase, I.; Nakamura, M.; Namatame, H.; Fujishima, Y.; Tokura, Y.; Abbate, M.; de Groot, F. M. F.; Czyzyk, M. T.; Fuggle, J. C.; Strebel, O.; Lopez, F.; Domke, M.; Kaindl, G. Doping-induced Changes in the Electronic Structure of $La_x Sr_{1-x}TiO_3$: Limitation of the One-electron Rigid-band Model and the Hubbard Model. *Phys. Rev. B* **1992,** *46* (15), 9841-9844.

56.	Itoh, T.; Shirasaki, S.; Ofuchi, H.; Hirayama, S.; Honma, T.; Nakayama, M. Oxygen Partial Pressure Dependence of In Situ X-ray Absorption Spectroscopy at the Co and Fe K Edges for $(La_{0.6}Sr_{0.4})(Co_{0.2}Fe_{0.8})O_{3-\delta}$. *Solid State Commun.* **2012,** *152* (4), 278-283.

57.	Carvalho, M. D.; Ramos, T.; Ferreira, L. P.; Wattiaux, A. Mixed Valence States of Cr and Fe in $La_{1-x}Sr_xFe_{0.8}Cr_{0.2}O_{3-y}$. *Solid State Sci.* **2010,** *12* (4), 476-481.

58.	Yao, W.; Duan, T.; Li, Y.; Yang, L.; Xie, K. Perovskite Chromate Doped with Titanium for Direct Carbon Dioxide Electrolysis. *New J. Chem.* **2015,** *39* (4), 2956-2965.

59.	Yokokawa, H.; Horita, T.; Sakai, N.; Yamaji, K.; Brito, M. E.; Xiong, Y. P.; Kishimoto, H. Thermodynamic Considerations on Cr Poisoning in SOFC cathodes. *Solid State Ionics* **2006,** *177* (35-36), 3193-3198.

60.	Yamahara, K.; Jacobson, C. P.; Visco, S. J.; Zhang, X.-F.; De Jonghe, L. C. Thin Film SOFCs with Cobalt-infiltrated Cathodes. *Solid State Ionics* **2005,** *176* (3–4), 275-279.

61.	Liu, W.; Konysheva, E. Y. Conductivity of $SrCrO_4$ and Its Influence on Deterioration of Electrochemical Performance of Cathodes in Solid Oxide Fuel Cells. *ECS Trans.* **2014,** *59* (1), 327-332.

62.   Karim, D. P.; Aldred, A. T. Localized Level Hopping Transport in La(Sr)CrO$_3$. *Phys. Rev. B* **1979,** *20* (6), 2255-2263.

63.   Wei, T.; Liu, X.; Yuan, C.; Gao, Q.; Xin, X.; Wang, S. A Modified Liquid-phase-assisted Sintering Mechanism for La$_{0.8}$Sr$_{0.2}$Cr$_{1-x}$Fe$_x$O$_{3-\delta}$—A High Density, Redox-Stable Perovskite Interconnect for Solid Oxide Fuel Cells. *J. Power Sources* **2014,** *250* (0), 152-159.

64.   Rembelski, D.; Viricelle, J. P.; Combemale, L.; Rieu, M. Characterization and Comparison of Different Cathode Materials for SC-SOFC: LSM, BSCF, SSC, and LSCF. *Fuel Cells* **2012,** *12* (2), 256-264.

65.   Takeda, Y.; Kanno, R.; Noda, M.; Tomida, Y.; Yamamoto, O. Cathodic Polarization Phenomena of Perovskite Oxide Electrodes with Stabilized Zirconia. *J. Electrochem. Soc.* **1987,** *134* (11), 2656-2661.

66.   Armstrong, E. N.; Duncan, K. L.; Wachsman, E. D. Effect of A and B-site Cations on Surface Exchange Coefficient for ABO$_3$ Perovskite Materials. *Phys. Chem. Chem. Phys.* **2013,** *15* (7), 2298-2308.

67.   Yoo, J.; Verma, A.; Wang, S.; Jacobson, A. J. Oxygen Transport Kinetics in SrFeO$_{3-\delta}$, La$_{0.5}$Sr$_{0.5}$FeO$_{3-\delta}$, and La$_{0.2}$Sr$_{0.8}$Cr$_{0.2}$Fe$_{0.8}$O$_{3-\delta}$ Measured by Electrical Conductivity Relaxation. *J. Electrochem. Soc.* **2005,** *152* (3), A497-A505.

68.   Ramos, T.; Atkinson, A. Oxygen Diffusion and Surface Exchange in La$_{1-x}$Sr$_x$Fe$_{0.8}$Cr$_{0.2}$O$_{3-\delta}$ (x=0.2, 0.4 and 0.6). *Solid State Ionics* **2004,** *170* (3–4), 275-286.

69.   Read, M. S. D.; Saiful Islam, M.; Watson, G. W.; King, F.; Hancock, F. E., Defect Chemistry and Surface Properties of LaCoO. *J. Mater. Chem.* **2000,** *10* (10), 2298-2305.

70.   Fujita, K. Prevention of SOFC Cathode Degradation in Contact with Cr-containing Alloy. In *8th Grove Fuel Cell Symposium*, Elsevier Science Publisher B.V. : London, England, **2003**.

TOC graphic